Extreme Mechanics Letters 49 (2021) 101503

Contents lists available at ScienceDirect

Extreme Mechanics Letters

journal homepage: www.elsevier.com/locate/eml

Strain gradient plasticity modeling of nanoindentation of additively manufactured stainless steel

Kunqing Ding [a,1], Yin Zhang [a,1], Andrew J. Birnbaum [b], John G. Michopoulos [b]
David L. McDowell [a], Ting Zhu [a,*]

[a] George W. Woodruff School of Mechanical Engineering, Georgia Institute of Technology, Atlanta, GA 30332, USA
[b] US Naval Research Laboratory, Washington, DC 20375, USA

ARTICLE INFO

Article history:
Received 11 September 2021
Received in revised form 9 October 2021
Accepted 10 October 2021
Available online 27 October 2021

Keywords:
Additive manufacturing
Nanoindentation
Strain gradient plasticity
Finite element
Size effect

ABSTRACT

Nanoindentation can be used to probe the mechanical behavior of additively manufactured materials, but requires a fundamental understanding of inhomogeneous deformation and size effects at the various length scales involved. Here we perform gradient plasticity finite element (GPFE) simulations of nanoindentation of additively manufactured stainless steel layers on stainless steel baseplates. The GPFE simulation results, when compared with their experimental nanoindentation counterparts, capture the size dependence of indentation hardness arising from strong plastic strain gradients developed at small indentation depths. Furthermore, they address the strengthening effects due to the interplay of several characteristic length scales involved, including the indentation depth, the grain size, and the size of printing-induced dislocation cells. This work demonstrates that GPFE simulations can be effectively applied for quantitative evaluation and mechanistic understanding of the nanoindentation behavior of additively manufactured materials.

1. Introduction

Additive manufacturing, also called three-dimensional (3D) printing, is a powerful approach for direct production of end-use parts in automotive, aerospace, biomedical and other industries. Additive manufacturing of metal alloys via laser powder bed fusion (L-PBF) features highly localized melting, strong temperature gradients, and rapid cooling [1]. These extreme printing conditions often result in non-equilibrium microstructures such as printing-induced dislocation cells inside grains, leading to mechanical properties that can be markedly different from their counterparts produced by conventional routes [2,3]. Nanoindentation enables the probing of mechanical behavior of 3D-printed materials [4,5]. However, an effective use of nanoindentation testing results requires a fundamental understanding of inhomogeneous deformation and size effects associated with the nanoindentation of 3D-printed materials over multiple length scales.

This work focuses on nanoindentation of laser-melted 316L stainless steel single tracks. We have previously conducted nanoindentation testing of as-printed stainless steel on stainless steel baseplates with different grain sizes [4,5]. Based on these nanoindentation results, we apply in this work a recently developed strain gradient plasticity theory [6] to perform finite element simulations of nanoindentation. The simulation results allow us to not only estimate the uniaxial stress–strain response of indented materials, but also capture the micro/nano-indentation size effect, namely, an increase of indentation hardness with decreasing indentation depth. Such indentation size effect is generally known to arise from the extra strengthening of plastic strain gradients at small indentation depths [7,8], which can be affected by the non-equilibrium microstructure in 3D-printed alloys. As illustrated in Fig. 1, our gradient plasticity finite element (GPFE) modeling is able to capture the strengthening effects of several characteristic length scales involved during nanoindentation of 3D-printed stainless steel [4,5], including the depth of the nanoindenter δ in the range of tens of nanometers to a few microns, the size of printing-induced dislocation cells d of a few hundred nanometers in size, and the grain size D ranging from a few microns to over a hundred microns. Understanding the interplay of these deformation and microstructure length scales has broader implications for investigation of nanoindentation behavior of additively manufactured materials in the future.

2. Methods

2.1. Experimental

Here we provide a brief overview of 3D printing and nanoindentation testing of austenitic 316L stainless steel, as reported

* Corresponding author.
E-mail address: ting.zhu@me.gatech.edu (T. Zhu).
[1] These authors contributed equally.

https://doi.org/10.1016/j.eml.2021.101503
2352-4316/

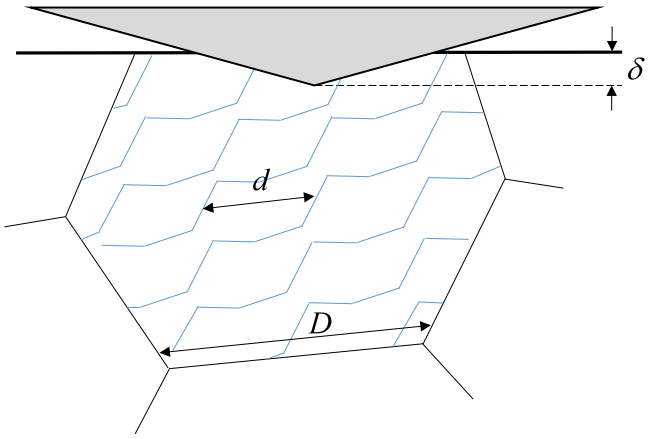

Fig. 1. Schematic illustration of interplay of several characteristic length scales involved during nanoindentation testing of a 3D-printed alloy, including the depth of the nanoindenter δ, the size of printing-induced dislocation cells (enclosed by blue lines) d, and the size of grains (enclosed by black lines) D. (For interpretation of the references to color in this figure legend, the reader is referred to the web version of this article.)

by Birnbaum et al. [4,5]. Their nanoindentation testing results provide a basis for the present GPFE study. As described in detail by Birnbaum et al. [4], single-track 316L stainless steel samples from L-PBF were chosen as model sample configurations (Fig. 2) in order to minimize the complexities associated with building larger objects, and thus multiple melt/re-melt and heat/re-heat cycles. All single tracks were processed directly on a 5 mm thick 316L baseplate. Two types of baseplate were used. One is the as-received baseplate having a grain size of $\sim$ 10 μm, while the other is the annealed baseplate with a grain size of $\sim$ 400 μm. They are referred to as small grain baseplate (SG_BP) and giant grain baseplate (GG_BP), respectively. Since the printed layer has a tendency of epitaxial growth from the baseplate [4,5], its grain characteristics, including grain size and orientation, largely follow those of the baseplate (Fig. 2). The printed layers on SG_BP and GG_BP are referred to as small grain laser-processed (SG_LP) and giant grain laser-processed (GG_LP), respectively. The grains in these single tracks contain a number of printing-induced dislocation cells of a few hundred nanometers in size [4,5], which can elevate both the yield strength and the rate of work hardening of as-printed materials. As shown in Fig. 2(a), nanoindentation tests were performed on the polished side surface of both baseplates and printed layers, including the four cases of GG_BP, GG_LP, SG_BP, and SG_LP, using a Hysitron indenter equipped with a Berkovich tip. In this work, we focus on the representative indenter force versus depth response for each case. As shown in [5], the error bars of indentation measurements at different locations for each case are small, which imply the relatively weak effects of local structural variation on the measured hardness values. A comparative study of these four cases allows us to assess how nanoindentation behavior is affected by grain sizes in baseplates and printed layers as well as sub-structural features arising from additive manufacturing, such as printing-induced dislocation cells.

2.2. Strain gradient plasticity theory

Past experiments have established the micro/nano-indentation size effect of crystalline metals [7,8]. The principal origin of this size effect is associated with plastic strain gradients developed beneath a stiff indenter. In this work, we use a strain gradient plasticity theory [6] to represent the nonlinear strengthening effect of nanoindentation-induced plastic strain gradients. In this gradient plasticity theory, the classical J_2 theory is extended by incorporating plastic strain gradients into a hardening rate relation. Hence, higher order stresses and additional boundary conditions are not needed, allowing the micro/nano-indentation size effect to be captured with minimal complexity in theory and implementation.

In the following, several key constitutive relations in the strain gradient plasticity theory [6] are given, while additional formulation is provided in the Appendix. In this theory, the uniaxial equivalent plastic strain rate $\dot{\epsilon}^p$ at a given temperature is given by a power-law relation

$$\dot{\varepsilon}^{\mathrm{p}} = \dot{\varepsilon}_0^{\mathrm{p}} \left(\frac{\overline{\sigma}}{s} \right)^{1/m} \tag{1}$$

where $\dot{\varepsilon}_0^{\mathrm{p}}$ is the reference plastic strain rate, m is the strain rate sensitivity, $\overline{\sigma}$ is the uniaxial equivalent stress, and s is the plastic flow resistance. Note that s has an initial value of s_0 corresponding to the yield strength of the material, and it increases with the accumulated effective plastic strain $\overline{\varepsilon}^{\mathrm{p}} = \int_0^t \dot{\overline{\varepsilon}}^{\mathrm{p}} \mathrm{d}t'$ as well as a scalar measure of plastic strain gradients. That is, we take the following hardening rate relation

$$\dot{s} = h \dot{\overline{\varepsilon}}^{\mathrm{p}} \tag{2}$$

where h is the hardening rate coefficient given by

$$h = \frac{h_0}{1 + \left(\overline{\varepsilon}^{\mathrm{p}} / \varepsilon_1 \right)^{n_1}} \left[1 + \frac{\kappa \sqrt{\alpha}}{1 + \left(\overline{\varepsilon}^{\mathrm{p}} / \varepsilon_2 \right)^{n_2}} \right] \tag{3}$$

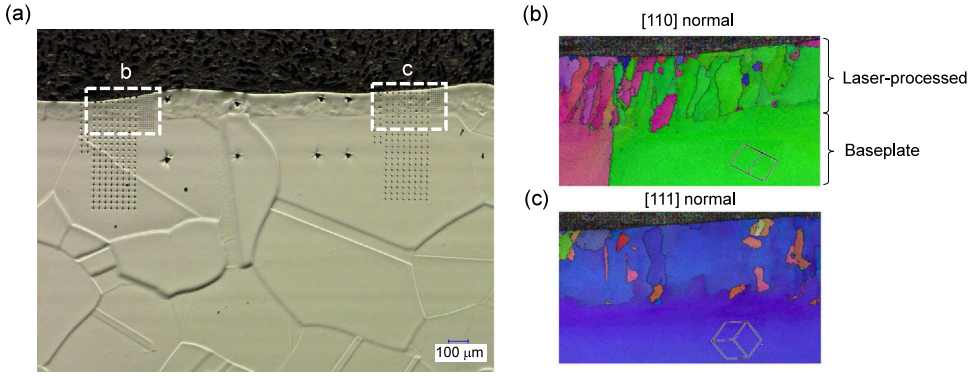

Fig. 2. Nanoindentation testing of 3D-printed stainless steel. (a) Optical micrograph showing nanoindentation arrays on a longitudinal section of a single-track printed layer on a baseplate with giant grains. (b, c) Inverse pole figure (IPF) map at different locations marked in (a), showing grain orientations in the baseplate and laser-processed layer, respectively.

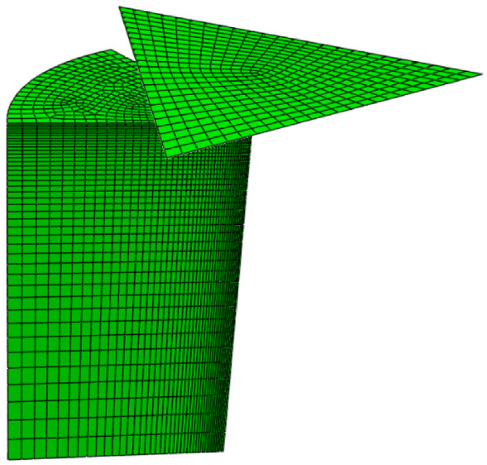

Fig. 3. Finite element setup for nanoindentation simulation.

In Eq. (3), h_0 is the hardening rate constant; ε_1 and n_1 govern the nonlinear strain hardening as a function of $\overline{\varepsilon}^{\mathrm{p}}$ in the absence of plastic strain gradients, and α is defined as

$$\alpha = \sqrt{\overline{\varepsilon}^{\mathrm{p}}_{,i}\overline{\varepsilon}^{\mathrm{p}}_{,i}} \tag{4}$$

which is a scalar measure of spatial gradients of $\overline{\varepsilon}^{\mathrm{p}}$, i.e., $\overline{\varepsilon}^{\mathrm{p}}_{,i} = \partial\overline{\varepsilon}^{\mathrm{p}}/\partial x_i$. Hence, the second term inside the square bracket of Eq. (3) represents the hardening contribution due to plastic strain gradients. Correspondingly, κ, ε_2 and n_2 are the parameters characterizing the nonlinear hardening effect of plastic strain gradients. When ε_2 is taken to be much smaller than ε_1, the hardening effect due to plastic strain gradients through α is strong if $\overline{\varepsilon}^{\mathrm{p}} < \varepsilon_2$. As $\overline{\varepsilon}^{\mathrm{p}}$ exceeds ε_2, the effect of plastic strain gradients decreases quickly and thus becomes negligible. It follows that the hardening effect is dominated by plastic strain accumulation.

2.3. Nanoindentation simulation

We employ a 3D finite element model (Fig. 3) to simulate the nanoindentation response to a Berkovich indenter in ABAQUS/CAE [9]. The Berkovich tip is a three-sided pyramid having a three-fold symmetry. Considering this symmetry, the simulation cell of the indented material is composed of 1/6 of a cylinder with a radius of 21 μm and height of 35 μm. The simulation cell is meshed with 26,544 elements of the C3D8 type. Each element has eight integration points, allowing the finite-difference calculation of plastic strain gradients within the element. These elements are graded with a fine mesh close to the surface that contacts the indenter. We implement the strain gradient plasticity theory described in Section 2.2 by developing a user hardening subroutine VUHARD in ABAQUS/EXPLICIT [9]. The Berkovich indenter is modeled as a three-sided pyramid and is assigned the elastic properties of diamond, i.e., Young's modulus of 2,440 GPa and Poisson's ratio of 0.2. A friction coefficient of 0.3 is assumed for the simulation of contact interaction between the indenter and substrate by utilizing a penalty method [9]. It has been previously shown that the use of different friction coefficients has a negligible effect on the simulation result of indentation force P versus depth δ [10]. Appropriate traction and displacement boundary conditions are prescribed for the indenter and substrate. From the simulated P-δ results, the indentation hardness H is calculated by $H = P/A$, where A is the contact area. To a first approximation for the Berkovich indenter, we assume $A = 24.675\delta^2 + 0.562\delta + 0.003216$ [11] and thus neglect the effect of indentation pile-up or sink-in on A.

3. Results and discussion

3.1. Size-independent hardness at large indentation depths

Nix and Gao [7] used the concept of geometrically necessary dislocations to account for the size dependence of indentation hardness. On this basis, they derived a relationship between the indentation hardness H and depth δ

$$\left(\frac{H}{H_0}\right)^2 = 1 + \frac{\delta^*}{\delta} \tag{5}$$

where H_0 is the hardness in the limit of infinite depth and δ^* is a characteristic length that depends on the shape of the indenter. It has been shown that the Nix–Gao relation in Eq. (5) can capture the δ-dependence of H when δ is around 1 μm and above [12]. In this work, we use Eq. (5) to extract the size-independent indentation hardness H_0 from the experimental data of δ versus H in the range of $\delta > 1$ μm. The H_0 value is dictated by the bulk mechanical properties of an indented material in the absence of indentation size effect.

More specifically, according to Eq. (5), H_0 can be determined by first making a linear fit of the nanoindentation testing data of $1/\delta$ versus H^2 and then extrapolating the linear fitting curve to intersect the axis of H^2, such that the intercept gives H_0^2. Fig. 4 shows the experimental data of $1/\delta$ versus $(H/H_0)^2$ (black line) as well as the linear fitting curve (red line) for the four cases of GG_BP, GG_LP, SG_BP, and SG_LP. The corresponding H_0 values are determined as 1.40 GPa, 1.49 GPa, 1.76 GPa and 1.94 GPa, respectively. Comparison of these H_0 values indicates that the giant grains ($\sim$ 400 μm in size) of the baseplate (GG_BP) give the lowest H_0, while the printing-induced dislocation cells in the giant grains of the printed layer (GG_LP) cause a slight increase of H_0. Compared to the printing-induced dislocation cells (GG_LP), the small grains (10 μm in size) in the baseplate (SG_BP) can lead to a larger increase of H_0, suggesting a more pronounced strengthening effect of the grain boundaries associated with small grains in SG_BP than the dislocation cells in GG_LP. Finally, the printing-induced dislocation cells in the small grains of the printed layer (SG_LP) give the largest H_0, suggesting the strongest strengthening effect of the grain boundaries associated with small grains together with the printing-induced dislocation cells in SG_LP. Overall, this comparative study of the four cases demonstrates the strengthening effects to various extents on H_0 due to the reduced grain size and/or the presence of printing-induced dislocation cells, as illustrated in Fig. 1.

3.2. Estimation of uniaxial stress–strain curve

Based on the H_0 value for each case given above, we estimate the corresponding uniaxial stress–strain curve of the indented material in the absence of plastic strain gradient. To solve this inverse problem, we attempt to achieve a good match of H_0 between the predicted value from a finite element simulation of size-independent indentation hardness with the corresponding experimental value. That is, we ignore the effect of plastic strain gradient by setting $\kappa = 0$ in the hardening rate relation of Eq. (3) in this part of study. It follows that the simulated indentation hardness values associated with the geometrically self-similar indents produced by the Berkovich tip with increasing depth remain constant independent of δ. For a given experimental H_0 value for an indented material, we estimate its plastic parameters s_0, h_0, ε_1, n_1 using the effective stress concept. According to Johnson [13], the hardness measured by a Berkovich or a Vickers indenter can be related to three times the effective tensile stress at a tensile strain of 7%. On this basis, we refine our estimate of the effective tensile stress by a series of nanoindentation

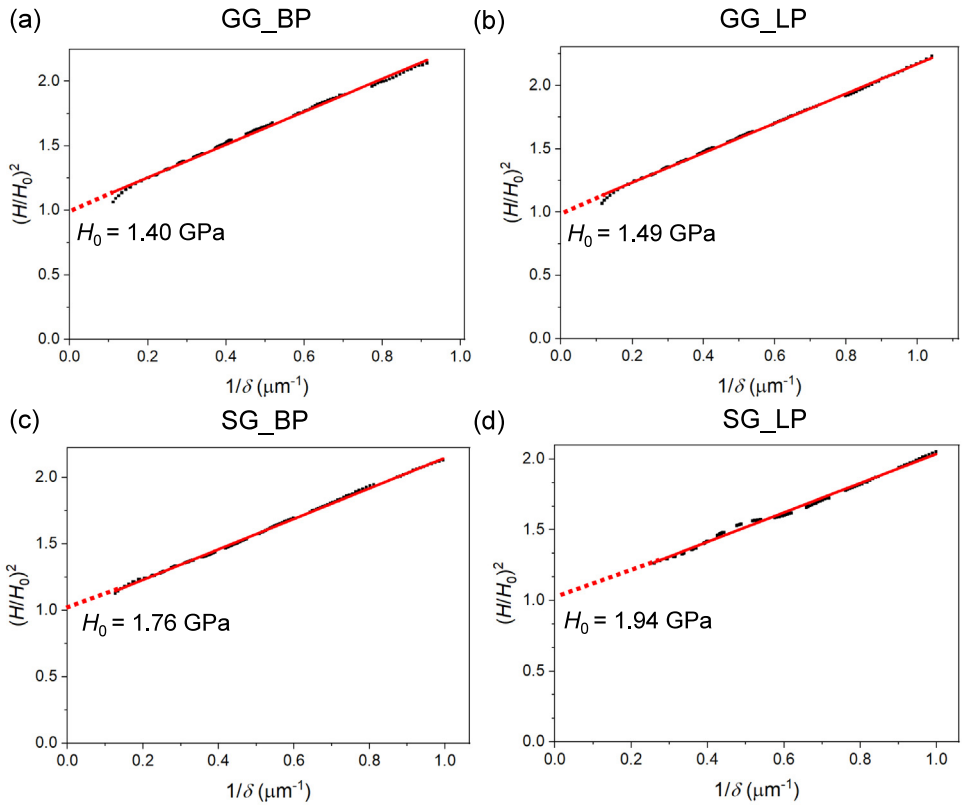

Fig. 4. Experimentally measured nanoindentation hardness H^2 is plotted as a function of inverse of indentation depth δ (black line) for the four cases of GG_BP, GG_LP, SG_BP, and SG_LP (a-d). The size-independent indentation hardness H_0 for each case is extracted at $1/\delta = 0$ from the corresponding linear fitting curve (red line). (For interpretation of the references to color in this figure legend, the reader is referred to the web version of this article.)

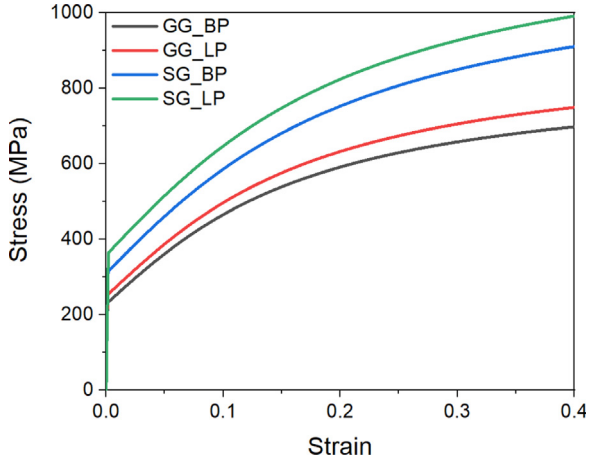

Fig. 5. Uniaxial tensile stress–strain curves determined from solving an inverse problem through the finite element simulation of size-independent indentation for the four cases of GG_BP, GG_LP, SG_BP, and SG_LP.

simulations. Namely, we take $H_0/3$ as the effective tensile stress at a tensile strain, then adjust the corresponding parameters of h_0, ε_1, n_1 to run a finite element simulation of indentation for a simulated value of H_0. A series of nanoindentation simulations indicate that $H_0/3$ can be taken as the effective tensile stress at a tensile strain of 10%, such that the simulated value of H_0 gives a close match (less than 3% difference) with the experimental value of H_0.

Using the above procedure, we obtain the uniaxial stress–strain curve of the indented material for all four cases of GG_BP, GG_LP, SG_BP, and SG_LP, as shown in Fig. 5. The corresponding

Table 1
Parameters used in the strain gradient plasticity model for the four cases of GG_BP, GG_LP, SG_BP, and SG_LP.

	s_0 (MPa)	h_0 (MPa)	ε_1	n_1	κ ($\sqrt{\text{m}}$)	$\varepsilon_2(\times 10^{-5})$	n_2
GG_BP	232	2842	0.128	1.83	194.9	2.4	3
GG_LP	253	2947	0.133	1.83	236.6	2.7	16
SG_BP	315	3198	0.153	1.78	234.5	1.8	10
SG_LP	364	3330	0.156	1.8	264.6	2.2	20

plastic parameters of s_0, h_0, ε_1, n_1 are listed in Table 1. Similar to the earlier results in Section 3.1 showing the effects of grain size and printing-induced dislocation cells on H_0, the giant grains in the baseplate (GG_BP) give the overall softest stress–strain curve, while the small grains in the printed layer (SG_LP) lead to the overall hardest stress–strain curve. In addition, the printing-induced dislocation cells in the printed layer with giant grains (GG_LP) elevate the stress–strain curve relative to the baseplate with giant grains (GG_BP), while the reduced grain size in the baseplate (SG_BP) leads to a much larger elevation of the stress–strain curve relative to the printed layer with giant grains (GG_LP). Overall, this comparative study of the four cases shows the effects of extra strengthening on uniaxial stress–strain behavior due to the reduced grain sizes and/or printing-induced dislocation cells.

We note that the above procedure enables a simplified yet reasonable estimate of uniaxial stress–strain behavior of the indented material, considering the estimated stress–strain responses of baseplates (GG_BP and SG_BP) are consistent with those of 316 stainless steel in the literature [14,15]. However, this procedure relies only on the size-independent indentation hardness of H_0 and thus cannot give a unique inverse solution of the uniaxial stress–strain curve. In other words, if the effective

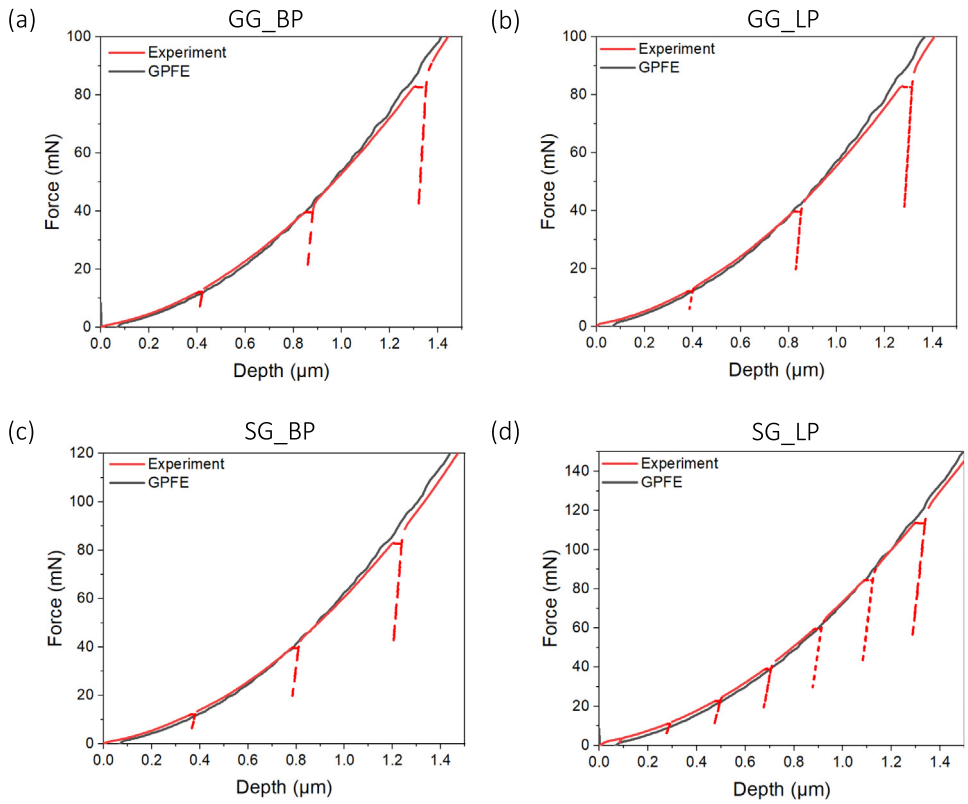

Fig. 6. Comparison of nanoindentation force versus depth curves between experiments and CPFE simulations for the four cases of GG_BP, GG_LP, SG_BP, and SG_LP. Red dashed lines represent unloading segments in experiments.

tensile stress were to be taken at a tensile strain somewhat different from 10%, the simulated value of H_0 from the modified parameters of h_0, ε_1, n_1 could also match the experimental value of H_0 with similar accuracy. Hence, a rigorous inverse solution of the uniaxial stress–strain curve should be pursued in future work along the lines of Dao et al. [16]; this requires a more complex procedure with additional input from the size-independent indentation testing results.

3.3. Size-dependent nanoindentation behavior

Using the plastic parameters determined in Section 3.2, we perform GPFE simulations of size-dependent nanoindentation behavior for all four cases of GG_BP, GG_LP, SG_BP, and SG_LP. In each case, the gradient-dependent plastic parameters in Eq. (3), including κ, ε_2 and n_2, are determined through matching the simulation and experimental results of size-dependent nanoindentation behavior at small indentation depths. Table 1 lists the fitting parameters of κ, ε_2 and n_2 for all four cases. Fig. 6 shows the simulated indentation force versus depth curves, which agree closely with the corresponding experimental curves. Furthermore, Fig. 7 shows the simulated indentation hardness versus depth curves which also agree with the corresponding experimental curves. Hence, our GPFE model enables quantitative simulations of size-dependent nanoindentation hardness, despite increased discrepancy for very small indentation depths less than ~ 0.2 μm. The oscillations of the simulated indenter force in Fig. 7 arise because there are a relatively small number of elements in contact with the indenter tip at small indentation depths. As the indenter is moved downward, it will come into contact with more elements and thus more nodes. The resultant redistribution of nodal forces in the contact elements causes the oscillations of the indenter force. Such oscillations can be reduced with increasing mesh density. The dashed lines in Figs. 6 and 7 indicate nanoindentation unloading segments in experiments. They are not simulated in this work and warrant further modeling studies in the future.

To understand the results of size-dependent nanoindentation hardness, we first provide a brief overview of the related mechanistic analysis by Lim and Chaudhri [17] and then discuss the impact of microstructure induced by 3D printing. Based on a series of nanoindentation experiments of annealed and strain-hardened Cu, Lim and Chaudhri [17] suggest that the nanoindentation size effect at small indentation depths less than 150 nm is mainly controlled by nucleation of dislocation loops [18]. These loops are mostly geometrically necessary dislocations generated to accommodate plastic strain gradients developed around the indenter tip. These geometrically necessary dislocations give rise to high hardening rates at small indentation depths, leading to a strong size-strengthening effect. For larger indentation depths, the dislocation loops expand and glide beneath the indenter. Hardness decreases with increasing indentation depth due to lower stress needed to expand loops of larger diameters. For still larger indentation depths, those dislocations interact with each other and form more complex patterns, giving a weaker strengthening effect owing to reduced plastic strain gradients and accordingly decreased density of geometrically necessary dislocations with increasing indentation depth.

While the mechanistic analysis by Lim and Chaudhri [17] is generally applicable to the size-dependent nanoindentation response in 3D-printed stainless steel, our comparative nanoindentation study for the four cases suggests some extra strengthening effects due to the interplay of nanoindentation-induced dislocations with printing-induced dislocations as well as with grain boundaries associated with giant or small grains. Such interplay is influenced strongly by their characteristic length scales involved [4,5], including the depth of the nanoindenter δ in the range of tens of nanometers to a few microns, the grain size D ranging from a few microns to over a hundred

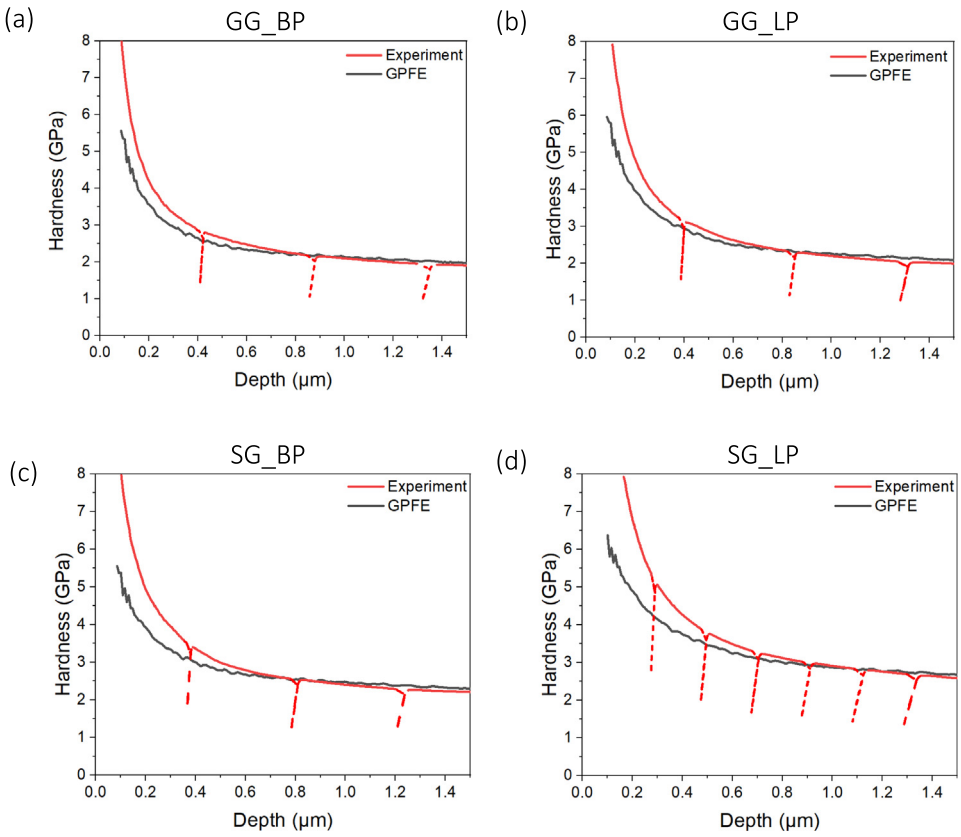

Fig. 7. Comparison of nanoindentation hardness versus depth curves between experiments and CPFE simulations for the four cases of GG_BP, GG_LP, SG_BP, and SG_LP. Red dashed lines represent unloading segments in experiments.

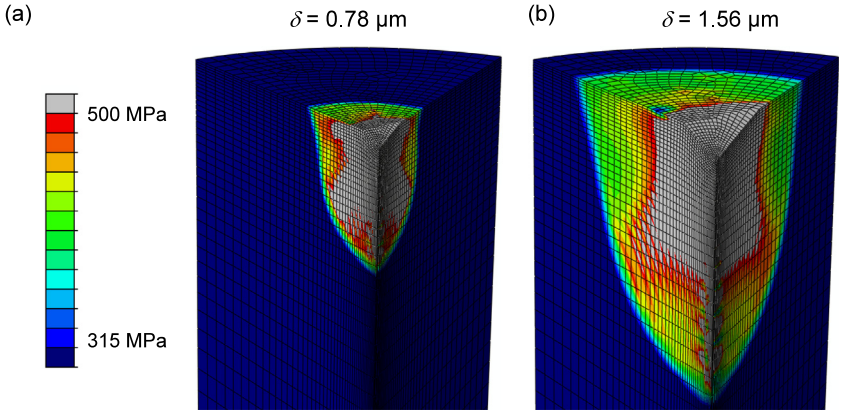

Fig. 8. Contours of von Mises stresses from GPFE simulations of nanoindentation in GG_BP at the indentation depth (a) $\delta = 0.78\,\mu m$ and (b) $\delta = 1.56\,\mu m$, respectively.

microns, and the size of printing-induced dislocation cells d of a few hundred nanometers, as illustrated in Fig. 1. More specifically, it is seen that compared to GG_BP (Fig. 7(a)), the size-dependent indentation hardness is enhanced to similar extent in GG_LP (Fig. 7(b)) and SG_BP (Fig. 7(c)). These results suggest that the extra strengthening effect due to interaction between the nanoindentation-induced dislocations and the printing-induced dislocations is close to that arising from interaction between the nanoindentation-induced dislocations and the grain boundaries associated with small grains. In addition, Fig. 7(d) indicates that the size-dependent indentation hardness can be enhanced to the largest extent in SG_LP. This effect can be attributed to the extra strengthening that is promoted greatly through strong interaction among the nanoindentation-induced dislocations, the printing-induced dislocations, and the grain boundaries associated with the smallest grains among the four cases studied. To further understand these interactions, we note that Ma et al. [19] recently show the transmission electron microscopy images of nanoindentation-induced dislocation structures at different indentation depths of Ni crystals. It would be helpful to perform a similar study as that of Ma et al. [19] in the future, in order to directly correlate the evolution of dislocation structures in baseplates and printed layers with the corresponding size-dependent nanoindentation hardness response.

To further reveal the impact of plastic strain gradients on size-dependent indentation hardness, Fig. 8 shows von Mises stress contours from a GPFE simulation of nanoindentation in GG_BP at two different indentation depths. The upper and lower limits of the contour scale bar are set to highlight the non-uniform

stress distribution in the transition region from elastic to plastic deformation where von Mises stresses are around the yield strength. Since the effect of plastic strain gradients is accounted for in this GPFE simulation, these von Mises stress contours are no longer self-similar with increasing indentation depth. Instead, the elastic–plastic transition region exhibits a relatively larger fraction of red domain of high von Mises stresses at a smaller indentation depth of $\delta = 0.78$ μm, as opposed to a relatively larger fraction of green domain of low von Mises stresses at a larger indentation depth of $\delta = 1.56$ μm. This difference gives rise to a stronger strengthening effect associated with larger plastic strain gradients at a smaller indentation depth, as shown by a higher indentation hardness of 2.20 GPa at the depth of 0.78 μm compared to 1.96 GPa at the depth of 1.56 μm. In the future, it would be helpful to correlate the GPFE study of spatially varying plastic strain gradients in baseplates and printed layers with the corresponding transmission electron microscopy study of dislocation structures at different indentation depths along the lines of Ma et al. [19], as discussed above.

4. Conclusion

We have performed GPFE simulations of nanoindentation in 3D-printed stainless steel, as compared with our earlier nanoindentation testing results [4,5]. The conclusions and perspectives from this work are given below.

- Nanoindentation testing offers an effective means of probing the mechanical behavior of 3D-printed materials. GPFE simulation enables both quantitative evaluation and mechanistic understanding of the nanoindentation response of 3D-printed materials.
- A simplified method is developed to estimate the uniaxial stress–strain curve of an indented material. On this basis, GPFE simulation can be applied to evaluate the effect of plastic strain gradients on the size-dependent indentation hardness.
- Through a comparative study of 3D-printed stainless steel single-tracks and stainless steel baseplates with different grain sizes, the combined nanoindentation testing and GPFE simulation results reveal the strengthening effects arising from interplay of several characteristic length scales involved, including the depth of the nanoindenter δ in the range of tens of nanometers to a few microns, the size of printing-induced dislocation cells d of a few hundred nanometers in size, and the size of grains D ranging from a few microns to over a hundred microns. These results provide a valuable basis for in-depth investigation of the relationship between the mechanical behavior and underlying microstructure of 3D-printed materials in the future.
- Extreme thermomechanical conditions during additive manufacturing often lead to significant macroscale and microscale residual stresses in as-printed materials [2,3]. Such multiscale residual stresses can affect nanoindentation behavior and thus warrant future research. Broadly speaking, the combination of nanoindentation testing and GPFE simulation can be used as a coherent approach for high throughput mapping of local mechanical properties of 3D-printed parts with complex geometry and/or spatially varying composition and microstructure. Achieving this capability is important towards the ultimate goal of producing reliable 3D-printed parts in real-world applications.

Declaration of competing interest

The authors declare that they have no known competing financial interests or personal relationships that could have appeared to influence the work reported in this paper.

Acknowledgments

KD, YZ, TZ and DLM acknowledge support by the Office of Naval Research under the Agile ICME Toolkit project (N00014-18-1-2784). AJB and JGM acknowledge support by the Office of Naval Research through the Naval Research Laboratory's core funding, and the Office of Naval Research under the Agile ICME Toolkit project (N0001420WX00405).

Appendix

To supplement the key constitutive relations of the strain gradient plasticity theory in Section 2.2, we provide additional formulation in this appendix. In this gradient plasticity theory [6], the total infinitesimal strain rate tensor $\dot{\varepsilon}_{ij}$ is decomposed into elastic and plastic parts, i.e.,

$$\dot{\varepsilon}_{ij} = \dot{\varepsilon}^{\mathrm{e}}_{ij} + \dot{\varepsilon}^{\mathrm{p}}_{ij} \tag{A.1}$$

Assuming isotropic linear elasticity, the elastic strain rate $\dot{\varepsilon}^{\mathrm{e}}_{ij}$ is related to the stress rate $\dot{\sigma}_{ij}$ by the generalized Hooke's law

$$\dot{\varepsilon}^{\mathrm{e}}_{ij} = \frac{1}{E}\left[(1+\nu)\dot{\sigma}_{ij} - \nu\dot{\sigma}_{kk}\delta_{ij}\right] \tag{A.2}$$

where E is Young' modulus, ν is Poisson's ratio and repeated indices imply summation. Assuming plastic isotropy, the plastic strain rate $\dot{\varepsilon}^{\mathrm{p}}_{ij}$ follows the J_2 flow rule

$$\dot{\varepsilon}^{\mathrm{p}}_{ij} = \dot{\bar{\varepsilon}}^{\mathrm{p}}\frac{3\sigma'_{ij}}{2\bar{\sigma}} \tag{A.3}$$

where σ'_{ij} is the deviatoric stress and $\bar{\sigma}$ is the uniaxial equivalent stress defined by

$$\bar{\sigma} = \sqrt{\frac{3}{2}\sigma'_{ij}\sigma'_{ij}} \tag{A.4}$$

and $\dot{\bar{\varepsilon}}^{\mathrm{p}}$ is the equivalent plastic strain rate given by a simple power-law relation of Eq. (1).

References

[1] T. DebRoy, H.L. Wei, J.S. Zuback, T. Mukherjee, J.W. Elmer, J.O. Milewski, A.M. Beese, A. Wilson-Heid, A. De, W. Zhang, Additive manufacturing of metallic components - process, structure and properties, Prog. Mater. Sci. 92 (2018) 112–224.
[2] Y.M. Wang, T. Voisin, J.T. McKeown, J. Ye, N.P. Calta, Z. Li, Z. Zeng, Y. Zhang, W. Chen, T.T. Roehling, R.T. Ott, M.K. Santala, Philip J. Depond, M.J. Matthews, A.V. Hamza, T. Zhu, Additively manufactured hierarchical stainless steels with high strength and ductility, Nature Mater. 17 (2018) 63–71.
[3] W. Chen, T. Voisin, Y. Zhang, J.-B. Florien, C.M. Spadaccini, D.L. McDowell, T. Zhu, Y.M. Wang, Microscale residual stresses in additively manufactured stainless steel, Nature Commun. 10 (2019) 4338.
[4] A.J. Birnbaum, J.C. Steuben, E.J. Barrick, A.P. Iliopoulos, J.G. Michopoulos, Intrinsic strain aging, $\Sigma 3$ boundaries, and origins of cellular substructure in additively manufactured 316L, Addit. Manuf. 29 (2019) 100784.
[5] A.J. Birnbaum, H. Ryou, J.C. Steuben, A.P. Iliopoulos, K.J. Wahl, J.G. Michopoulos, Nested size effects in the nanoindentation response of additively manufactured 316L stainless steel, Mater. Lett. 280 (2020) 128570.
[6] Y. Zhang, Z. Cheng, L. Lu, T. Zhu, Strain gradient plasticity in gradient structured metals, J. Mech. Phys. Solids 140 (2020) 103946.
[7] W.D. Nix, H. Gao, Indentation size effects in crystalline materials: A law for strain gradient plasticity, J. Mech. Phys. Solids 46 (1998) 411–425.
[8] G.M. Pharr, E.G. Herbert, Y. Gao, The indentation size effect: A critical examination of experimental observations and mechanistic interpretations, Annu. Rev. Mater. Res. 40 (2010) 271–292.
[9] ABAQUS 6.13, User's Manual, SIMULIA, Providence, R.I., 2010.
[10] C.-M. Sanchez-Camargo, A. Hor, C. Mabru, A robust inverse analysis method for elastoplastic behavior identification using the true geometry modeling of Berkovich indenter, Int. J. Mech. Sci. 171 (2020) 105370.
[11] N.A. Sakharova, J.V. Fernandes, J.M. Antunes, M.C. Oliveira, Comparison.between. Berkovich, Vickers and conical indentation tests: A three-dimensional numerical simulation study, Int. J. Solids Struct. 46 (2009) 1095–1104.

[12] J.G. Swadener, E.P. George, G.M. Pharr, The correlation of the indentation size effect measured with indenters of various shapes, J. Mech. Phys. Solids 50 (2002) 681–694.
[13] K.L. Johnson, The correlation of indentation experiments, J. Mech. Phys. Solids 18 (1970) 115–126.
[14] X. Feaugas, On the origin of the tensile flow stress in the stainless steel AISI 316L at 300 K: Back stress and effective stress, Acta Mater. 47 (1999) 3617–3632.
[15] J. Hu, A.C.F. Cocks, A multi-scale self-consistent model describing the lattice deformation in austenitic stainless steels, Int. J. Solids Struct. 78–79 (2016) 21–37.
[16] M. Dao, N. Chollacoop, K.J. Van Vliet, T.A. Venkatesh, S. Suresh, Computational modeling of the forward and reverse problems in instrumented sharp indentation, Acta Mater. 49 (2001) 3899–3918.
[17] Y.Y. Lim, M.M. Chaudhri, The effect of the indenter load on the nanohardness of ductile metals: An experimental study on polycrystalline work-hardened and annealed oxygen-free copper, Phil. Mag. A 79 (1999) 2979–3000.
[18] J. Li, K.J. Van Vliet, T. Zhu, S. Yip, S. Suresh, Atomistic mechanisms governing elastic limit and incipient plasticity in crystals, Nature 418 (2002) 307–310.
[19] X. Ma, W. Higgins, Z. Liang, D. Zhao, G.M. Pharr, K.Y. Xie, Exploring the origins of the indentation size effect at submicron scales, Proc. Nat. Acad. Sci. USA 118 (2021) e2025657118.